Research Square

Preprints are preliminary reports that have not undergone peer review.
They should not be considered conclusive, used to inform clinical practice,
or referenced by the media as validated information.

Bypassing thermodynamic immiscibility via electrochemical kinetic atom trapping

Yuzhang Li

yuzhangli@ucla.edu

University of California, Los Angeles https://orcid.org/0000-0002-1502-7869

Min-Ho Kim

University of California Los Angeles

Jin Koo Kim

University of California, Los Angeles

Kaiyan Liang

University of California, Los Angeles

Hayoung Park

University of California Los Angeles

Tianyu Wang

University of California, Los Angeles https://orcid.org/0000-0002-8738-9869

Huida Lyu

University of California, Los Angeles https://orcid.org/0009-0000-1935-5117

Kaixi Chen

University of California, Los Angeles (UCLA) https://orcid.org/0000-0003-1561-9546

Dingyi Zhao

UCLA https://orcid.org/0009-0002-1854-6354

Jung Tae Kim

University of California, Los Angeles

Jinyoung Kim

University of California, Los Angeles

Article

Keywords:

Posted Date: November 6th, 2026

DOI: https://doi.org/10.21203/rs.3.rs-11136042/v1

License: This work is licensed under a Creative Commons Attribution 4.0 International License.
Read Full License

Additional Declarations: There is **NO** Competing Interest.

Bypassing thermodynamic immiscibility via electrochemical kinetic atom trapping

Min-Ho Kim[1,2,†,*], Jin Koo Kim[1,3,†], Kaiyan Liang[1,†], Hayoung Park[1,4], Tian-Yu Wang[1], Huida Lyu[1], Kaixi Chen[1], Dingyi Zhao[1], Jung Tae Kim[1], Jinyoung Kim[1], Yuzhang Li[1,*]

[1]Department of Chemical and Biomolecular Engineering, University of California, Los Angeles (UCLA); Los Angeles, CA 90095, USA

[2]Present address: Department of Energy Engineering, Korea Institute of Energy Technology; Naju 58330, Republic of Korea

[3]Present address: Advanced Cell Research Center, LG Energy Solution; Daejeon 34122, Republic of Korea

[4]Present address: Department of Chemical Engineering and Materials Science, Ewha Woman's University; Seoul 03760, Republic of Korea

†These authors contributed equally

*Corresponding author. Email: minhokim@kentech.ac.kr, yuzhangli@ucla.edu

Abstract

Immiscible elemental pairs can access properties unavailable to equilibrium solid solutions, but conventional synthesis approaches suffer from phase separation and heterogeneity. Here, we establish kinetic atom trapping using ultramicroelectrodes, confining metal-ion reduction to a finite interfacial inventory. Ultrahigh-, ultrashort-current pulses deplete the preferentially reduced ion before radial diffusion replenishes the interface, forcing dissimilar ions to reduce concurrently and kinetically trapping and stabilizing homogeneous immiscible nanoalloys. The strategy produces mixed nanoparticles across diverse atomic combinations, such as Cu–Zn, Cu–Ag, Cu–Fe, Fe–Cr, and Cu–Ni systems. A quantitative pulse window, bounded by Sand's depletion time and radial-diffusion-mediated replenishment, predicts the current density and pulse duration required for co-reduction. These mechanistic design rules establish a route to metastable immiscible alloys and enable automated exploration of non-equilibrium compositions and properties.

Main Text

Metallic elemental pairs with positive enthalpies of mixing are generally regarded as immiscible[1–4]. This thermodynamic incompatibility, however, also makes them compelling targets for materials design. Forcing such elements into a single, atomically mixed phase could, in principle, generate combinations of properties inaccessible to conventional alloys, ranging from multifunctional structural responses to strained catalytic surface sites with enhanced activity[4–7].

The central barrier is primarily thermodynamic. A positive enthalpy of mixing favors phase separation as the lowest-energy state, such that processes operating near equilibrium drive immiscible elements apart rather than together[8]. Conventional solidification and thermal alloying proceed on timescales sufficiently long for compositional fluctuations to relax toward this equilibrium state[4,7,9]. Consequently, these approaches rarely access the homogeneous single-phase compositions required to realize such synergistic properties potentially hidden in immiscible alloys.

Overcoming this thermodynamic barrier requires kinetic strategies that outpace phase separation. Previously, ultrafast Joule heating has established that millisecond heating and quenching can trap otherwise immiscible elements in mixed nanoparticles before diffusion-driven segregation occurs[4,7]. However, compositional retention can be difficult to control because volatile constituents may be lost and the heating rate, peak temperature, dwell time and cooling rate are intrinsically coupled. These limitations motivate a kinetic approach in which the reaction rate and duration can be programmed more independently and precisely.

As an alternative, electrochemical deposition offers a complementary and potentially more controllable route to alloy formation[10–12]. In principle, if metal-ion reduction can be driven faster than surface diffusion and phase separation, atomically mixed immiscible alloys should form directly at the electrode[13], with the added advantage that the driving force, current density, is a continuously and precisely tunable experimental parameter linked directly to reaction kinetics[14,15]. Unlike thermal routes, however, electrochemical alloy formation faces an additional, distinct bottleneck before the problem of phase separation arises: ions with different reduction potentials do not naturally reduce or incorporate at the same rate. Under conventional electrodeposition conditions, the more readily reduced ion is preferentially deposited, while the less readily reduced ion remains in solution or is incorporated only after the local electrochemical environment has changed. Thus, even for metals that could in principle form a mixed phase, a reduction potential mismatch can lead to ion selective deposition or sequential deposition rather than concurrent co-reduction. For immiscible pairs, electrochemical synthesis must therefore solve two coupled problems: (1) synchronizing the reduction of dissimilar metal ions and (2) preventing the reduced atoms from undergoing thermodynamic de-mixing.

In this work, we establish kinetic atom trapping at ultramicroelectrodes (UMEs) as a route to override both reduction-potential mismatch and thermodynamic de-mixing across diverse immiscible pairs (Fig. 1a). The small dimensions of the customized UMEs (25 μm in diameter)

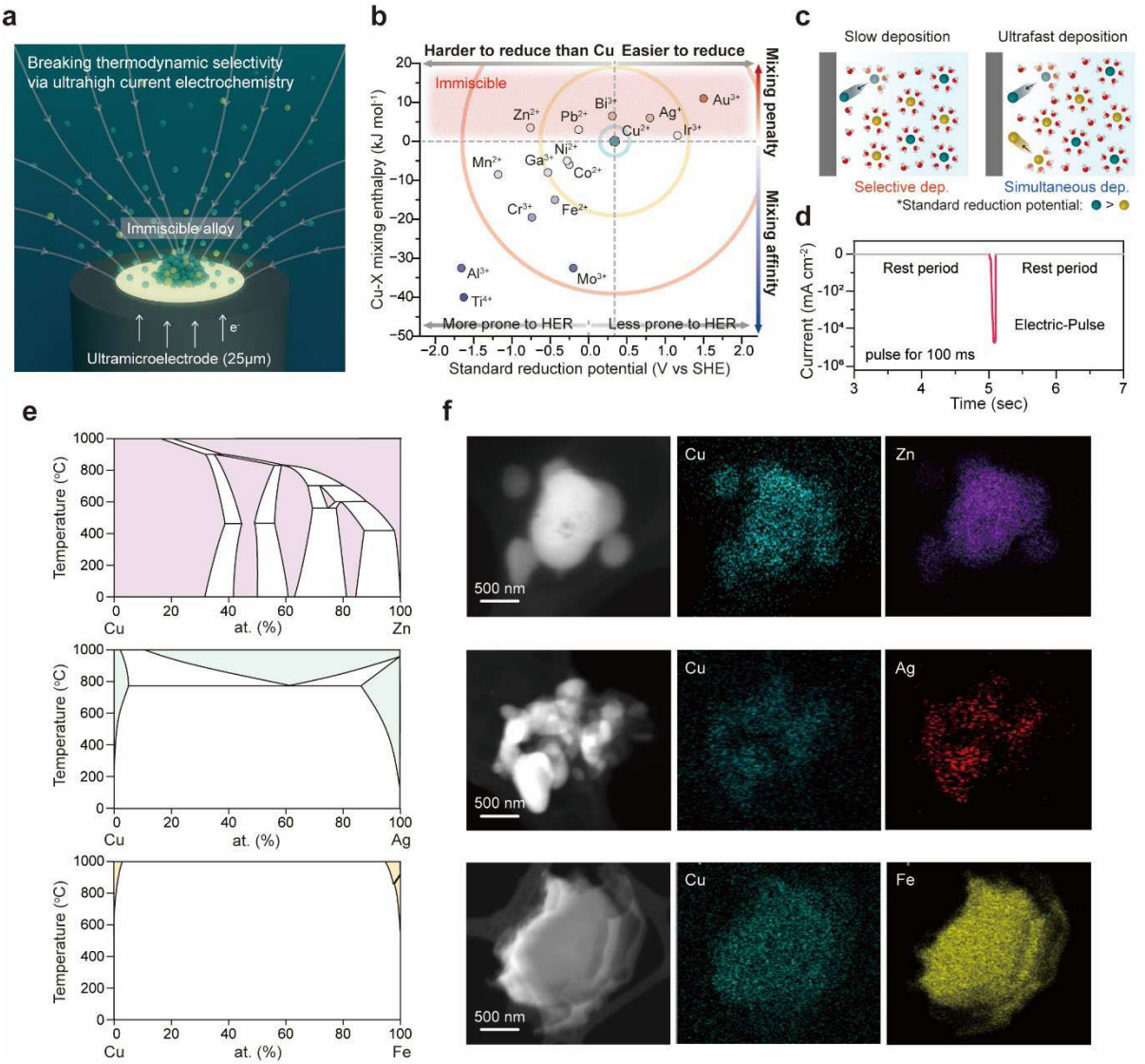


Fig. 1. Kinetic atom trapping enables electrochemical alloying beyond bulk miscibility. a, Conceptual illustration of kinetic atom trapping at a 25-μm-diameter ultramicroelectrode (UME), where ultrahigh current density drives rapid reduction of metal ions within a confined near-electrode reaction volume. **b**, Map of Cu–X mixing enthalpy as a function of standard reduction potential for representative metal ions. Positive mixing enthalpy identifies thermodynamically immiscible Cu–X pairs, whereas increasing separation from Cu in reduction potential represents a progressively larger electrochemical barrier to concurrent reduction. Concentric circles indicate increasing reduction-potential mismatch relative to Cu. **c**, Schematic comparison of conventional slow deposition and ultrafast deposition. Slow deposition preferentially consumes the more readily reduced ion, resulting in selective deposition, whereas rapid depletion of the interfacial ionic inventory enables simultaneous reduction of dissimilar ions during ultrafast deposition. **d**, Representative current-pulse protocol consisting of an ultrahigh-current pulse separated by rest periods. **e**, Equilibrium binary phase diagrams of Cu–Zn, Cu–Ag, and Cu–Fe, representing systems with distinct equilibrium phase behavior and alloying constraints. **f**, STEM images and corresponding elemental maps of Cu–Zn, Cu–Ag, and Cu–Fe particles synthesized by pulsed UME electrodeposition. Spatially overlapping elemental distributions demonstrate concurrent incorporation of the constituent metals despite their thermodynamic and electrochemical incompatibilities.

minimize iR drop and support radial diffusion, enabling ultrahigh current densities and access to electrochemical phenomena on millisecond timescales that are inaccessible at conventional macroscopic electrodes (Supplementary Fig. 1)[16–18]. Rather than relying on ultrahigh current density alone, the strategy exploits a defined kinetic window: the pulse must persist long enough to deplete the preferentially reduced ion and force concurrent reduction, yet terminate

before radial diffusion replenishes the interface. We quantify this window using characteristic depletion and replenishment times, thereby providing a predictive and quantitative basis for selecting current density and pulse duration across dissimilar metal-ion pairs. Within this window, ions are co-reduced from the same confined interfacial inventory and kinetically trapped as homogeneous metastable nanoalloys. We further demonstrate support-integrated Cu–Ag nanoalloys as a proof-of-concept electrocatalyst and establish the physical basis for future automated, high-throughput exploration of non-equilibrium alloy compositions.

Transient co-reduction at ultramicroelectrodes.

Figure 1b maps representative elements relative to Cu according to two fundamental barriers to electrochemical alloying: (1) the difference in standard reduction potential and (2) the Cu–X mixing enthalpy. The horizontal axis measures the reduction potential offset from Cu, whereas the vertical axis represents the thermodynamic driving force for mixing. Elements with positive mixing enthalpies lie in the immiscible regime, where conventional alloying processes favor phase separation rather than formation of a homogeneous alloy. Even for thermodynamically miscible pairs with negative mixing enthalpies, a large reduction potential mismatch, shown in concentric circles (blue: 0.2 V, yellow: 1.0 V, and red: 2.0 V), makes their simultaneous reduction intrinsically difficult under even conventional electrochemical conditions, instead leading to selective deposition of the more readily reduced species. Indeed, binary alloy electrodeposition is itself a well-established research topic, encompassing complex interactions between metal-ion reduction kinetics, mass transport, and phase formation[11,19–21].

To overcome these two bottlenecks simultaneously, we hypothesized that an ultrahigh-, ultrashort -current pulses could transiently isolate a confined interfacial reaction volume and consume the ions initially present within this volume before they are differentially replenished from the bulk electrolyte (Fig. 1c). Under conventional slow deposition, the more readily reduced species is preferentially consumed at the electrode surface, progressively shifting the local interfacial composition and resulting in selective deposition. In contrast, when a sufficiently large number of electrons is delivered over a timescale shorter than bulk mass transport, both ionic species can be incorporated within a short transient window before their distinct reduction tendencies establish compositional separation. We accessed this transient non-equilibrium regime using UMEs, which are suitable for imposing ultrahigh current densities over ultrashort durations (Fig. 1d)[22], where the short, high-current pulse confines the reaction to the early-time interfacial regime before bulk ions can replenish the electrode surface.

Guided by the reduction potential mixing enthalpy map and the corresponding equilibrium phase diagrams, we selected Cu–Zn, Cu–Ag, and Cu–Fe as representative systems spanning distinct alloying constraints (Fig. 1b,e). Cu–Zn contains several equilibrium intermediate phases, yet its positive mixing enthalpy and reduction potential separation exceeding 1 V impose thermodynamic and electrochemical barriers to homogeneous electrodeposition. By contrast, Cu–Ag and Cu–Fe exhibit no equilibrium intermediate phases, representing more stringent cases of immiscibility. Their electrochemical outcomes are further expected to

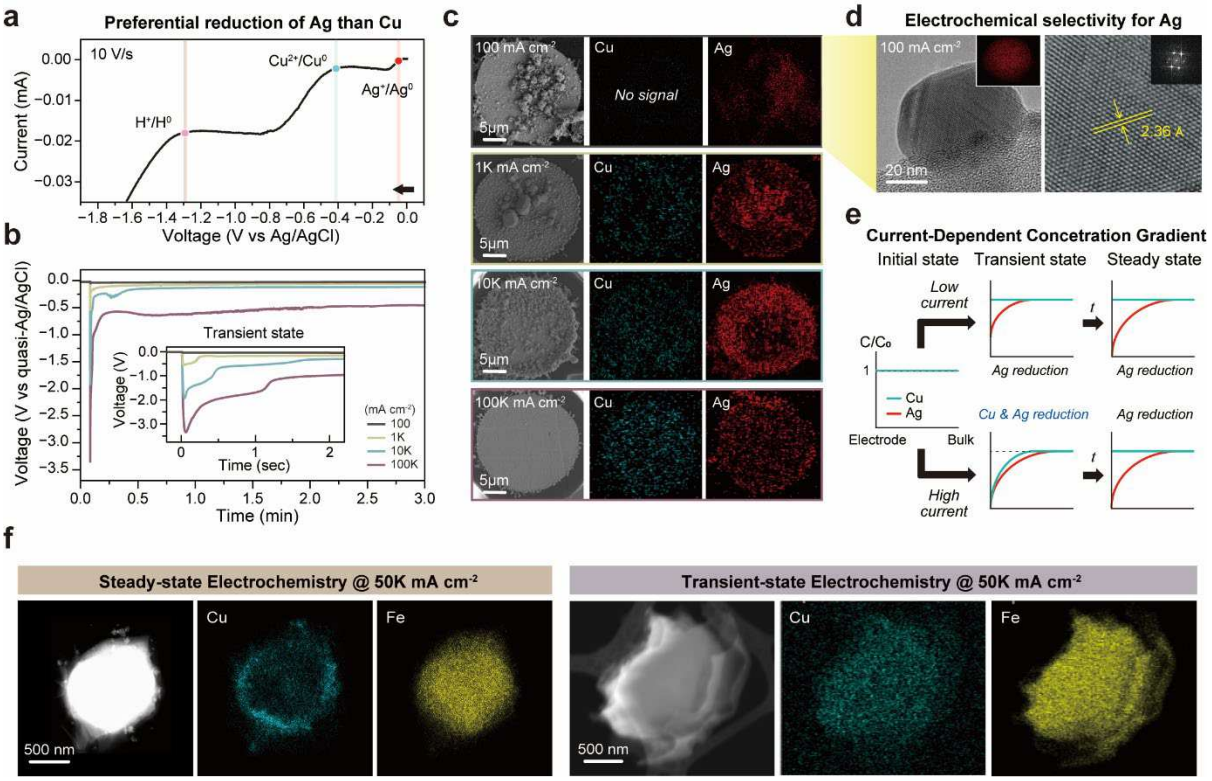


Fig. 2. Current- and time-dependent evolution of electrochemical selectivity during alloy deposition. a, Linear sweep voltammogram of the mixed Cu^{2+}/Ag^{+} electrolyte acquired at 10 V s^{-1}, showing the electrochemical separation between Ag^{+} and Cu^{2+} reduction and the onset of hydrogen evolution. **b**, Galvanostatic voltage transients for Cu–Ag deposition at current densities from 100 to 100,000 mA cm^{-2}. The inset highlights the first 2 s after current application, revealing the strongly current-dependent transient polarization preceding the longer-time quasi-steady-state response. **c**, SEM images and corresponding Cu and Ag elemental maps of deposits formed under continuous galvanostatic deposition at 10^2, 10^3, 10^4, and 10^5 mA cm^{-2}. Increasing current density progressively promotes Cu incorporation as rapid Ag^{+} depletion forces Cu^{2+} to participate in charge transfer. **d**, TEM characterization of the Ag-selective deposit obtained at 100 mA cm^{-2}. The Ag elemental map, lattice spacing of 2.36 Å, and corresponding FFT pattern are consistent with crystalline fcc Ag. **e**, Schematic evolution of the interfacial Cu^{2+} and Ag^{+} concentration profiles. At low current density, Ag^{+} alone sustains the imposed current and Ag-selective deposition persists. At sufficiently high current density, rapid Ag^{+} depletion forces transient Cu^{2+} reduction; subsequent bulk Ag^{+} replenishment during radial quasi-steady-state diffusion restores Ag-selective deposition. **f**, STEM images and elemental maps of Cu–Fe deposits formed at 50,000 mA cm^{-2} under steady-state and transient-state conditions. Prolonged deposition produces spatially segregated Cu- and Fe-rich regions, whereas transient deposition yields broadly overlapping Cu and Fe distributions.

diverge under conventional deposition conditions: Ag should preferentially deposit in the Cu–Ag system because of its more positive reduction potential, whereas Cu should dominate deposition in the Cu–Fe system because Fe reduction is substantially less favorable. Despite these distinct thermodynamic and electrochemical constraints, kinetic atom trapping approach successfully yielded particles in which both constituent elements were uniformly co-localized across the deposited nanostructures (Fig. 1f). These results demonstrate that the pulse-driven strategy can kinetically access homogeneously mixed phases even in alloy systems for which conventional electrochemical deposition would be expected to yield phase separation or single-element-dominated deposition.

Current- and time-dependency of Cu–Ag deposition

In the Cu–Ag system, linear sweep voltammetry (LSV) shows that the Ag^{+}/Ag reduction process occurs at a markedly more positive potential than the Cu^{2+}/Cu couple (Fig. 2a). This

large separation indicates that, under conventional galvanostatic deposition, Ag^+ should be preferentially reduced at the electrode interface. Cu^{2+} reduction is therefore expected to remain strongly suppressed until the local Ag^+ concentration is substantially depleted, such that the applied current can no longer be sustained predominantly by Ag deposition. In other words, conventional current-driven deposition should proceed through a temporally separated sequence with initial Ag-rich deposition followed by Cu incorporation only after Ag^+ exhaustion, rather than through the concurrent reduction required for homogeneous Cu–Ag alloy formation.

To elucidate the current-density-dependent electrochemical response, we performed galvanostatic measurements over four orders of magnitude in applied current density, from 100 to 100,000 mA cm^{-2} (Fig. 2b and Supplementary Fig. 2). The voltage response comprises an initial transient regime followed by a quasi-steady-state regime. Immediately after current application, the electrode potential changes rapidly as the electrical double layer is charged and the interfacial concentrations of electroactive species depart from their bulk values. During this early period, the diffusion layer grows from the electrode surface, and the concentration profile evolves continuously with time.

At early times, mass transport at the UME is effectively planar because the diffusion-layer thickness remains much smaller than the electrode radius[16,17]. As the diffusion layer expands to dimensions comparable to the UME radius, the transport field progressively transitions to hemispherical radial diffusion, enabling sustained replenishment of electroactive species from the surrounding electrolyte (Supplementary Fig. 3). Increasing the applied current density intensifies the early-time depletion of Ag^+ near the electrode surface, creating a transient window in which Cu^{2+} must contribute to the imposed current before radial quasi-steady-state transport is established.

Consistent with this expectation, deposition at 100 mA cm^{-2} produced no detectable Cu signal, whereas Ag was deposited exclusively (Fig. 2c). TEM analysis further identified the resulting particles as predominantly single-crystalline Ag, supported by uniform Ag mapping, lattice fringes with a spacing of 2.36 Å, and the corresponding FFT pattern characteristic of FCC Ag (Fig. 2d)[23]. This reduction-potential-driven selectivity is not unique to the Cu–Ag system. In contrast to Cu–Ag, where Ag is preferentially reduced, Cu possesses a substantially more positive reduction potential than Fe and Zn. Accordingly, continuous deposition at 100 mA cm^{-2} in the Cu–Fe and Cu–Zn systems produced deposits in which only Cu was detectably incorporated, whereas Fe and Zn signals were absent or negligible in the corresponding elemental maps (Supplementary Fig. 4). These results confirm that conventional galvanostatic deposition generally yields the more readily reduced metal, irrespective of the thermodynamic mixing characteristics of the alloy pair.

As the current density was increased to 10^3 and 10^4 mA cm^{-2}, Cu became increasingly detectable (Fig. 2c), indicating that local Ag^+ depletion forced Cu^{2+} to participate in charge transfer. Nevertheless, Ag remained the predominant deposited species under continuous

deposition, while the Cu was spatially segregated from Ag rather than forming a compositionally homogeneous alloy (Supplementary Fig. 5). Interestingly, when the current density was further increased to 10^5 mA cm^{-2}, this segregation was no longer apparent. Instead, Cu and Ag signals became broadly co-distributed across the deposited region (Fig. 2c), suggesting that ultrahigh-current deposition can suppress macroscopic Cu–Ag separation despite the intrinsic electrochemical selectivity between Ag^+ and Cu^{2+}. In particular, increasing the current density led to progressively smaller deposits, which may further facilitate compositional homogenization by shortening the characteristic diffusion length for elemental segregation (Fig. 2c and Supplementary Figs. 6 and 7)[24].

Fig. 2e summarizes the concentration-gradient evolution underlying this current-dependent transition. At low current density, Ag^+ reduction alone sustains the imposed current, leaving the Cu^{2+} concentration near the interface largely unchanged. At moderately high current densities, partial Ag^+ depletion enables Cu^{2+} reduction, but continuous Ag^+ replenishment from the bulk maintains an Ag-dominated interfacial flux, resulting in segregated Cu and Ag deposition. At 10^5 mA cm^{2-}, by contrast, Ag^+ is consumed faster than it can be replenished from the bulk, forcing both Ag^+ and Cu^{2+} within the finite near-electrode ionic inventory to participate in charge transfer during the early transient regime. However, as the diffusion field evolves toward a radial quasi-steady state, bulk Ag^+ replenishment restores Ag-selective growth and progressively suppresses Cu^{2+} reduction. These observations demonstrate that ultrahigh current density can access concurrent Cu–Ag reduction, but only within a short-lived transient window before electrochemical selectivity is re-established.

This transient-to-steady-state evolution of electrochemical selectivity is more directly visualized in the Cu–Fe system (Fig. 2f). Whereas steady-state deposition produced spatially segregated Cu- and Fe-rich regions, transient deposition led to broadly overlapping Cu and Fe distributions across the particle, indicating more homogeneous elemental mixing. The electrochemical response provides a mechanistic basis for this segregation (Supplementary Fig. 8). At the onset of deposition, the highly negative transient potential renders the reduction of both Cu and Fe electrochemically accessible, although the initial deposit appears predominantly Fe-rich, presumably owing to differences in reduction kinetics. As the potential relaxes upon entering the steady-state regime, Fe reduction is no longer sustained, leaving Cu as the predominant depositing species. Continued Cu deposition around the initially Fe-rich region consequently produces the Cu-rich exterior and Fe-rich interior observed under steady-state conditions.

A quantitative pulse-design window

We next established a physical framework to define the conditions required for concurrent reduction of ions with different reduction tendencies (Fig. 3a). Two criteria must be satisfied simultaneously. First, both ionic species at the electrode interface must be depleted within the pulse duration. In particular, the more readily reduced ion must be consumed rapidly enough that it can no longer solely sustain the applied current, thereby forcing reduction of the less noble counterpart. Second, the pulse must terminate before ions from the bulk electrolyte can

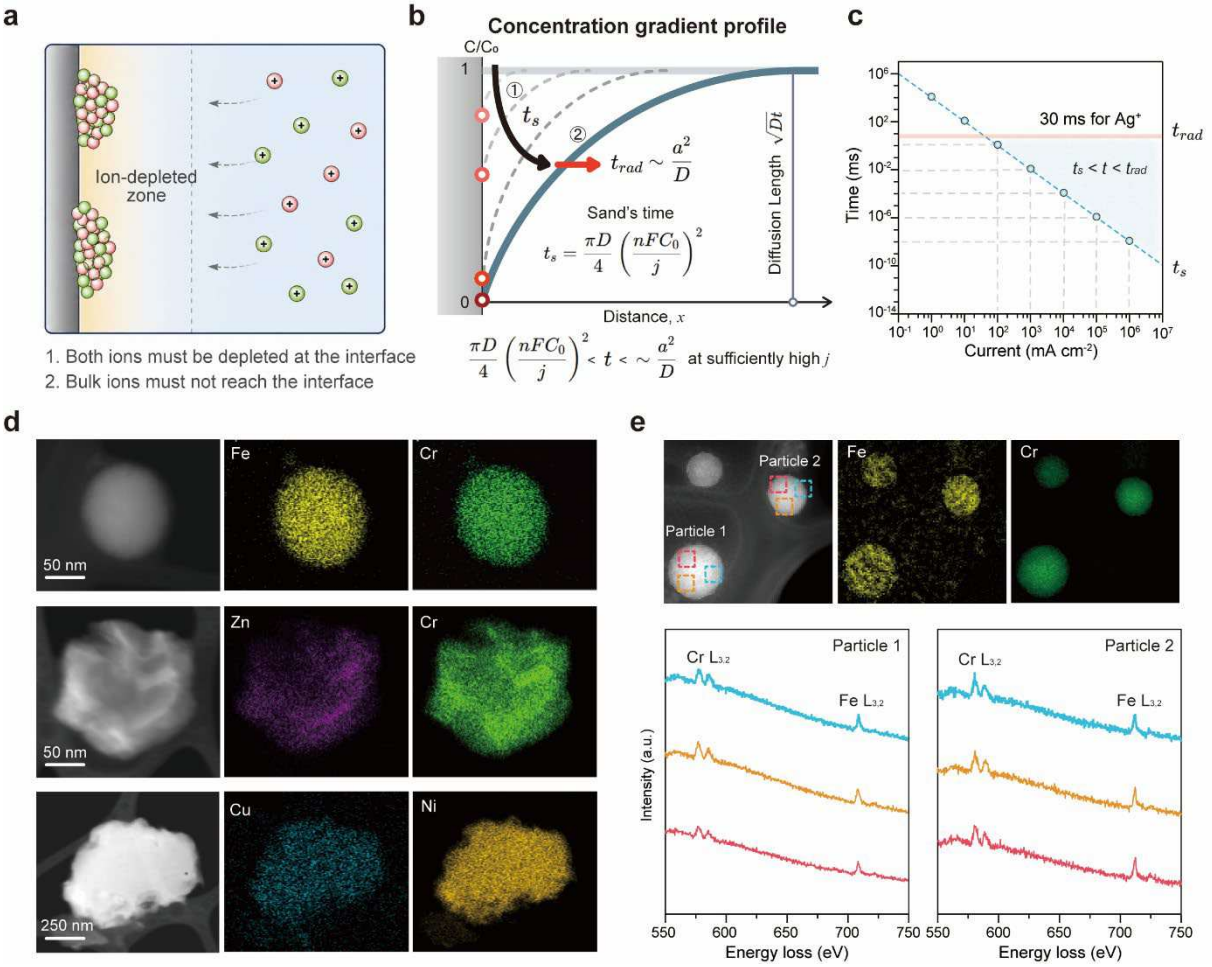


Fig. 3. Quantitative pulse window for transient co-reduction and extension to other alloy systems. a, Schematic illustration of the two experimental requirements for transient co-reduction: depletion of the preferentially reduced ion at the electrode interface and termination of the pulse before bulk ions replenish the reaction zone. **b**, Definition of the relevant time scales for pulse design. Sand's time estimates the time required for interfacial depletion of the preferentially reduced ion, whereas the radial-diffusion time estimates the onset of bulk replenishment at the UME. **c**, Calculated Sand's time and radial-diffusion time as a function of current density for the Cu–Ag system. The region between the two time scales defines the pulse-duration window in which Ag^+ is depleted but bulk replenishment has not yet restored Ag-selective deposition. **d**, STEM images and elemental maps of Fe–Cr, Zn–Cr, and Cu–Ni particles synthesized using pulsed UME electrodeposition. The overlapping elemental distributions indicate that the transient co-reduction condition can be applied to multiple binary systems. **e**, EELS spectra collected from different positions within Fe–Cr particles and from different particles. Similar Fe and Cr edge profiles across the sampled regions indicate local compositional uniformity and reproducibility of the pulse-synthesized Fe–Cr particles.

diffuse back to the interface and replenish the depleted reaction zone[25]. Only under these conditions can the reaction remain confined to a finite near-electrode ionic inventory, enabling concurrent reduction within the same transient interfacial volume.

To quantify this framework, we compared two characteristic timescales that bound the accessible pulse window (Fig. 3b). The lower bound is the interfacial depletion time, estimated using Sand's time, t_s, which describes the time required for the concentration of an electroactive ion at the electrode surface to approach depletion under galvanostatic, planar diffusion-limited conditions:

$$t_s = (\pi D/4)(nFC_0/j)^2$$

, where D is the ionic diffusivity, n is the number of electrons transferred per ion, F is the Faraday constant, C_0 is the bulk concentration of the electroactive ion and j is the applied current density[15,26]. Because Ag^+ is preferentially reduced over Cu^{2+} in the Cu–Ag system, Ag^+ depletion is the key event that must occur before Cu^{2+} reduction. Indeed, Sand derived this framework to account for the abrupt potential jump and subsequent onset of a secondary reaction (originally hydrogen evolution) once the primary electroactive species is depleted at the interface[26]. In our binary system, this interfacial depletion is similarly leveraged to trigger the reduction of the less noble counterpart. We therefore calculated t_s on the basis of Ag^+ depletion (Supplementary Fig. 9).

The upper bound, on the other hand, is the time required for bulk ions to diffuse over the characteristic UME length scale and replenish the depleted interfacial region. This timescale was approximated as

$$t_{rad} \approx a^2/D$$

, where a is the electrode radius, D is the ionic diffusivity, and subscript *rad* refers to the radial diffusion where bulk Ag ions reach the electrode surface[16,27]. This corresponds to the time at which the diffusion length becomes comparable to the electrode radius and the diffusion field begins to transition from early-time linear diffusion to the radial diffusion regime characteristic of UMEs (Supplementary Fig. 3). Once this regime is reached, bulk replenishment becomes efficient and the system approaches a quasi-steady-state current, restoring Ag-dominated selective deposition. Importantly, UME electrochemistry provides a direct experimental route to estimate ionic diffusivity, because the steady-state diffusion-limited current is well defined and can be related to ionic diffusivity under the same electrolyte and electrode geometry used in the experiment (Supplementary Fig. 10)[15–17]. Accordingly, concurrent Cu–Ag reduction is expected only when the pulse duration satisfies

$$t_s < t_{pulse} < t_{rad}$$

, such that interfacial Ag^+ has already been depleted, while bulk Ag^+ has not yet reached the reaction zone in sufficient quantity to restore selective deposition.

Figure 3c visualizes this criterion by plotting the calculated characteristic times as a function of current density. The Ag^+-based Sand's time decreases sharply with increasing current density, whereas the radial-diffusion timescale remains approximately constant at ~30 ms under the present UME geometry and electrolyte conditions. The blue shaded region therefore defines the pulse-design window in which the two requirements in Fig. 3a are simultaneously satisfied. At times shorter than t_s, Ag^+ is not yet sufficiently depleted and Ag-selective reduction persists. At times longer than t_{rad}, bulk Ag^+ replenishes the interface and the system reverts toward steady-state Ag-dominated deposition (Supplementary Fig. 11). Only within the shaded regime can the conventional electrochemical selectivity be bypassed, providing a

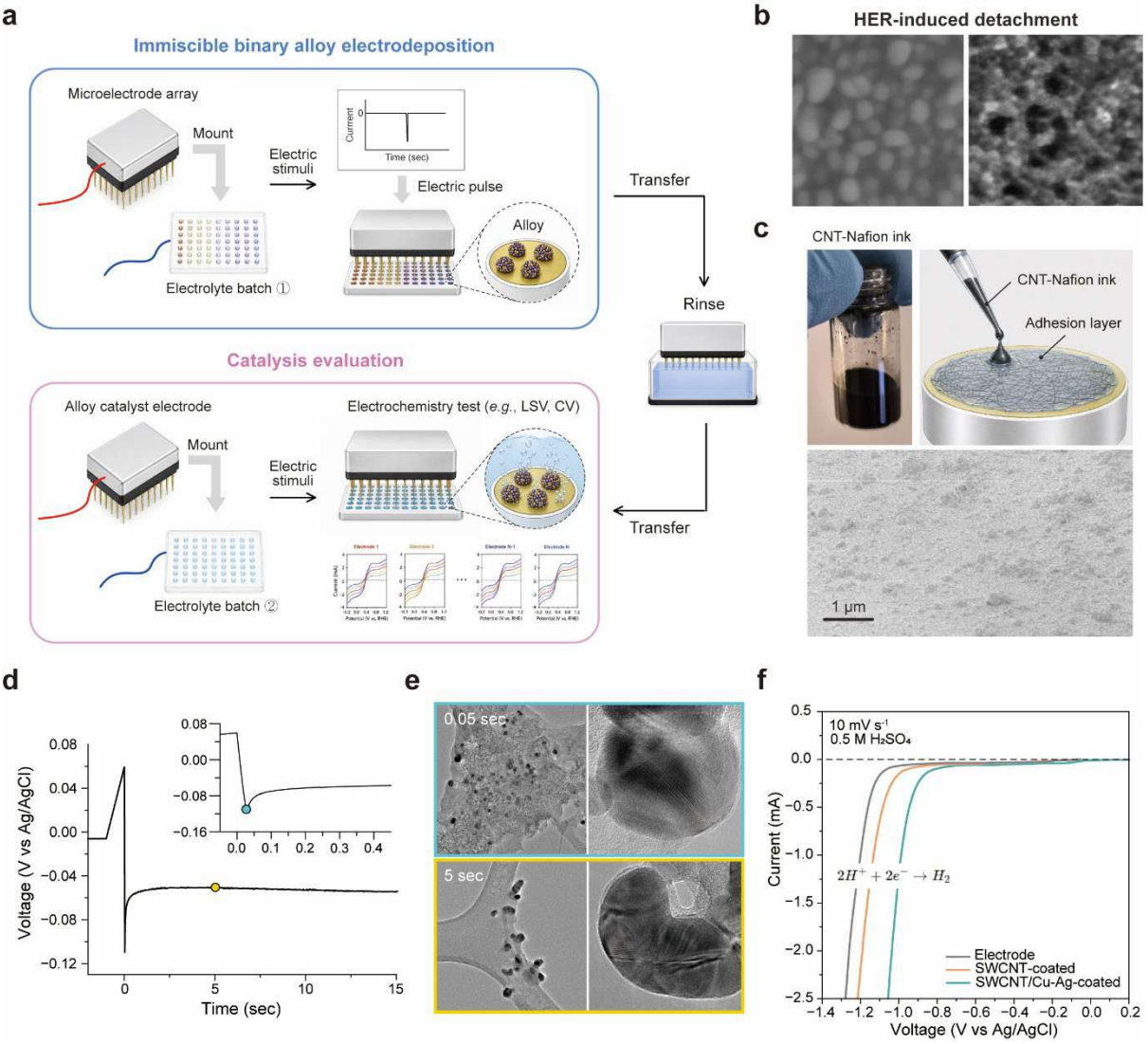


Fig. 4. Conceptual design of an automated high-throughput workflow. a, Conceptual automated workflow integrating immiscible-alloy electrodeposition with subsequent electrochemical evaluation. A microelectrode array is positioned over a compositionally varied precursor-electrolyte batch, subjected to programmed electrical pulses to generate an alloy library, rinsed, and transferred to a separate electrolyte batch for parallel catalytic testing. b, Representative scanning electron microscopic images demonstrating particle loss from an unsupported electrode during hydrogen-evolution conditions, highlighting the mechanical instability of weakly adhered deposits during gas evolution. c, CNT–Nafion support architecture used to improve particle retention, including a photograph of the CNT–Nafion ink, schematic illustration of coating formation on the electrode, and SEM image of the resulting carbon support layer. d, Galvanostatic potential transient during Cu–Ag deposition on the CNT–Nafion-coated electrode. Marked time points correspond to the short transient pulse and prolonged deposition conditions used for structural comparison. e, TEM images of deposits obtained after 0.05s and 5s deposition. The short pulse produces nanoscale Cu–Ag deposits on the carbon support, whereas prolonged deposition produces substantially larger Ag-rich crystalline particles. f, Hydrogen-evolution polarization curves measured at 10 mV s^{-1} in 0.5 M H_2SO_4 for bare electrode, SWCNT-coated electrode, and Cu–Ag-decorated SWCNT-coated electrode. The enhanced cathodic response of the supported Cu–Ag electrode demonstrates electrical integration and electrochemical accessibility of the pulse-synthesized alloy.

quantitative design rule for choosing current density and pulse duration to access non-equilibrium alloy formation.

Guided by this framework, we extended the pulse-design strategy to a broader range of binary systems with distinct elemental identities and alloying constraints (Fig. 3d). In each case,

ultrahigh, ultrashort pulse deposition produced particles with spatially overlapping elemental distributions, including Fe–Cr, Zn–Cr, and Cu–Ni, indicating that the framework is not limited to a specific redox pair but is broadly applicable across diverse elemental combinations. The resulting STEM-EDS maps show no obvious elemental segregation at the particle scale, demonstrating that the pulse window, we proposed, can generally drive concurrent incorporation of dissimilar ions into the same confined interfacial reaction volume.

In particular, we further examined the Fe–Cr system by EELS to assess chemical homogeneity at higher spatial resolution (Fig. 3e). Spectra acquired from different positions within a given particle, as well as from different particles, showed nearly identical Fe and Cr edge features and relative spectral profiles. The absence of position-dependent spectral variation indicates that the local composition is highly uniform throughout each particle, while the reproducibility across particles confirms that this uniformity is not an isolated event but a general outcome of the pulse-driven process. Together, these results provide strong evidence that the present framework enables the synthesis of chemically homogeneous alloys across multiple immiscible alloy systems.

Conceptual design of an automated high-throughput workflow

Having established pulse-enabled electrodeposition as a route to synthesize immiscible alloys, we next considered how this strategy could be extended beyond individual material synthesis toward an automated discovery workflow. As a proof of concept, we propose a hypothetical high-throughput platform that integrates parallel alloy electrodeposition with subsequent catalyst evaluation, thereby linking transient electrochemical synthesis directly to rapid functional screening (Fig. 4a). In this envisioned automated workflow, a robotic handler would precisely position a microelectrode array over a compositionally varied electrolyte batch, allowing each microelectrode to access a pre-defined precursor solution and receive programmed ultrahigh, ultrashort pulses. This arrangement could enable the parallel generation of distinct metastable alloy compositions under systematically varied electrolyte compositions and pulse parameters. The handler would then rinse the array and transfer it to a separate testing electrolyte, where the catalytic responses of the resulting alloy library could be evaluated in parallel under identical electrochemical conditions[28].

A key practical consideration is the mechanical stability of the deposited catalysts. Under ultrahigh current operation, vigorous hydrogen evolution and associated bubble formation can detach weakly adhered particles from the electrode surface (Fig. 4b and Supplementary Fig. 12). Moreover, practical electrocatalysts are commonly integrated with conductive carbon supports rather than used as unsupported metal particles. To address both considerations, we introduced a CNT–Nafion adhesion layer onto the microelectrode surface before alloy deposition (Fig. 4c)[29]. The interconnected CNT network provides a conductive, high-surface-area scaffold for particle anchoring, whereas Nafion promotes interfacial adhesion. Immiscible alloy growth was subsequently induced on this CNT–Nafion-coated surface, providing an electrode architecture designed to retain the pulse-synthesized particles during transfer, rinsing, and catalytic testing.

To validate this support-assisted deposition strategy, we compared long and transient deposition protocols on CNT–Nafion-coated electrodes (Fig. 4d). When plating was continued for 5 s, corresponding to the quasi-steady-state regime, discrete Ag single-crystalline particles were formed on the carbon support (Fig. 4e), consistent with the Ag-selective deposition observed under prolonged galvanostatic conditions. By contrast, limiting the deposition to a 0.05-s pulse confined the reaction to the transient regime and produced Cu–Ag alloy nanoparticles directly on the CNT-supported electrode surface, showing much smaller particle size.

As a proof-of-concept demonstration of catalyst integration, the transient Cu–Ag alloy was deposited onto a CNT-coated electrode and subsequently evaluated for hydrogen evolution in 0.5 M H_2SO_4 (Fig. 4f). Although detailed optimization of catalyst loading, support structure, electrolyte composition and testing parameters was beyond the scope of this study, the CNT-supported Cu–Ag alloy electrode exhibited an enhanced cathodic response relative to bare and CNT-coated control electrodes. This comparison demonstrates that the transiently synthesized alloy remains electrically accessible and catalytically active after integration with a practical carbon-supported electrode architecture, but is not intended to establish a composition-specific synergistic effect in the absence of corresponding single-metal Cu and Ag controls. More broadly, the result shows that pulse-driven immiscible alloy synthesis can be extended from unsupported particles on a model UME to support-integrated catalyst configurations suitable for downstream electrochemical evaluation.

Together, the UME-based physical framework, pulse-controlled alloy synthesis, and support-assisted catalyst integration establish a foundation for systematic exploration of non-equilibrium alloy compositions. While the present work does not implement a fully automated high-throughput screening platform, it defines the key physical and practical elements required for such a workflow: controlled transient depletion at UMEs, programmable access to metastable alloy compositions, and direct integration of the resulting materials onto conductive catalyst supports. By independently varying elemental precursors, current density, and pulse duration across a microelectrode array, this approach could ultimately enable high-throughput mapping of metastable alloy formation and catalytic performance across otherwise inaccessible compositional spaces.

Conclusion

In summary, we establish a kinetic atom trapping that confines metal-ion reduction to a finite interfacial inventory and thereby bypasses the reduction-potential-driven selectivity that normally prevents concurrent deposition of dissimilar ions. By leveraging the well-defined transient transport characteristics of UMEs, we define a quantitative kinetic window in which the pulse duration is bounded by the depletion time of the preferentially reduced ion and the onset of bulk-ion replenishment. This predictive framework, rather than ultrahigh current density alone, enables the rational selection of current density and pulse duration to access kinetically trapped, compositionally homogeneous alloys across chemically distinct and

otherwise difficult-to-co-deposit elemental pairs.

Beyond demonstrating metastable alloy formation, this work establishes the foundation for a broader materials-discovery strategy. The combination of UME-based transient electrochemistry, pulse-design rules, and support-integrated catalyst architectures provides a route toward systematic screening of non-equilibrium alloy compositions and their electrocatalytic properties. Although a fully automated high-throughput platform was not implemented here, the principles established in this study define the essential physical and practical basis for parallelized alloy synthesis, rapid compositional exploration, and catalyst discovery across vast elemental, compositional, and processing spaces.

References

1. Chen, P. C. *et al.* Complete miscibility of immiscible elements at the nanometre scale. *Nat. Nanotechnol.* **19**, 775–781 (2024).
2. Chen, W. *et al.* A map of single-phase high-entropy alloys. *Nat. Commun.* **14**, 2856 (2023).
3. Miracle, D. B. & Senkov, O. N. A critical review of high entropy alloys and related concepts. *Acta Mater.* **122**, 448–511 (2017).
4. Yao, Y. *et al.* Carbothermal shock synthesis of high-entropy-alloy nanoparticles. *Science* **359**, 1489–1494 (2018).
5. An, Z. *et al.* Negative mixing enthalpy solid solutions deliver high strength and ductility. *Nature* **625**, 697–702 (2024).
6. Meng, N. *et al.* High yield electrosynthesis of oxygenates from CO using a relay Cu-Ag co-catalyst system. *Nat. Commun.* **15**, 3892 (2024).
7. Yang, C. *et al.* Overcoming immiscibility toward bimetallic catalyst library. *Sci. Adv.* **6**, 1–9 (2020).
8. Tosun, İ. *The Thermodynamics of Phase and Reaction Equilibria*. (Elsevier, Amsterdam, 2013).
9. Ren, N. *et al.* Solute trapping and non-equilibrium microstructure during rapid solidification of additive manufacturing. *Nat. Commun.* **14**, 7990 (2023).
10. Leech, M. C. & Lam, K. A practical guide to electrosynthesis. *Nat. Rev. Chem.* **6**, 275–286 (2022).
11. Li, X. Electrodeposition of multi-component alloys: Thermodynamics, kinetics and mechanism. *Curr. Opin. Electrochem.* **39**, 101289 (2023).
12. Schlesinger, M. & Paunovic, M. *Fundamentals of Electrochemical Deposition*. (2006).
13. Philippe, T. Dynamics of phase separation of metastable crystal surfaces by surface diffusion: A phase-field study. *Phys. Rev. E* **110**, 034803 (2024).

14. Gileadi, E. *Electrode Kinetics for Chemists, Chemical Engineers, and Materials Scientists*. *Energy*.
15. ALLEN J. BARD, LARRY R. FAULKNER, H. S. W. *ELECTROCHEMICAL METHODS Fundamentals and Applications, 3rd*. (2022).
16. Heinze, J. Ultramicroelectrodes in Electrochemistry. *Angew. Chem. Int. Ed. Engl.* **32**, 1268–1288 (1993).
17. Forster, R. J. Microelectrodes: new dimensions in electrochemistry. *Chem. Soc. Rev.* **23**, 289 (1994).
18. Li, Y., Kim, M., Xie, Z., Min, J. & Li, Y. Microelectrodes for Battery Materials. *ACS Nano* **18**, 35119–35129 (2024).
19. Younes, O. & Gileadi, E. Electroplating of high tungsten content Ni/W alloys. *Electrochem. Solid-State Lett.* **3**, 543–545 (2000).
20. Younes, O., Zhu, L., Rosenberg, Y., Shacham-Diamand, Y. & Gileadi, E. Electroplating of amorphous thin films of tungsten/nickel alloys. *Langmuir* **17**, 8270–8275 (2001).
21. Gileadi, E. The enigma of metal deposition. *J. Electroanal. Chem.* **660**, 247–253 (2011).
22. Yuan, X., Liu, B., Mecklenburg, M. & Li, Y. Ultrafast deposition of faceted lithium polyhedra by outpacing SEI formation. *Nature* **620**, 86–91 (2023).
23. Guascito, M. R. *et al.* A new amperometric nanostructured sensor for the analytical determination of hydrogen peroxide. *Biosens. Bioelectron.* **24**, 1057–1063 (2008).
24. Pei, A., Zheng, G., Shi, F., Li, Y. & Cui, Y. Nanoscale Nucleation and Growth of Electrodeposited Lithium Metal. *Nano Lett.* **17**, 1132–1139 (2017).
25. Chandrasekar, M. S. & Pushpavanam, M. Pulse and pulse reverse plating—Conceptual, advantages and applications. *Electrochimica Acta* **53**, 3313–3322 (2008).
26. Sand, H. J. S. On the Concentration at the Electrodes in a Solution, with special reference to the Liberation of Hydrogen by Electrolysis of a Mixture of Copper Sulphate and Sulphuric Acid. *Proc. Phys. Soc. Lond.* **17**, 496 (1899).
27. Wightman, R. M. & Wipf, D. O. Voltammetry At Ultramicroelectrodes. in *Electroanalytical Chemistry* (CRC Press, 1988).
28. Lin, D.-Z. *et al.* A high-throughput experimentation platform for data-driven discovery in electrochemistry. *Sci. Adv.* **11**, 1–13 (2025).
29. Kuai, C. *et al.* Dissolved Fe species enable a cooperative solid – molecular mechanism for the oxygen evolution reaction on NiFe-based catalysts. *Nat. Catal.* https://doi.org/10.1038/s41929-025-01342-5 (2025) doi:10.1038/s41929-025-01342-5.

30. Perdew, J. P., Burke, K. & Ernzerhof, M. Generalized Gradient Approximation Made Simple. *Phys. Rev. Lett.* **77**, 3865–3868 (1996).

31. Blöchl, P. E. Projector augmented-wave method. *Phys. Rev. B* **50**, 17953–17979 (1994).

32. Kresse, G. & Furthmüller, J. Efficient iterative schemes for ab initio total-energy calculations using a plane-wave basis set. *Phys. Rev. B - Condens. Matter Mater. Phys.* **54**, 11169–11186 (1996).

Methods

Materials

Metal precursors used in this study include copper(II) nitrate trihydrate ($Cu(NO_3)_2 \cdot 3H_2O$), zinc nitrate hexahydrate ($Zn(NO_3)_2 \cdot 6H_2O$), iron(III) nitrate nonahydrate ($Fe(NO_3)_3 \cdot 9H_2O$), chromium(III) nitrate nonahydrate ($Cr(NO_3)_3 \cdot 9H_2O$), nickel nitrate hexahydrate ($Ni(NO_3)_2 \cdot 6H_2O$), silver nitrate ($AgNO_3$), iron(II) sulfate heptahydrate ($FeSO_4 \cdot 7H_2O$), and copper(II) sulfate pentahydrate ($CuSO_4 \cdot 5H_2O$).

Aqueous electrolytes were prepared using deionized (DI) water, with the concentration of each metal precursor fixed at 0.30 M unless otherwise specified. For each electrolyte, the required mass of each salt was calculated according to its molecular weight and the target solution volume. The salts were first completely dissolved in a small volume of DI water, after which additional DI water was added to reach the prescribed final volume. For binary-metal electrolytes, the required amounts of the two precursor salts were dissolved together using the same procedure, with each metal precursor maintained at 0.30 M. For Ag-containing electrolytes, a quasi-reference electrode was used instead of a conventional Ag/AgCl reference electrode to prevent chloride leakage from the reference electrode and the resulting precipitation of AgCl in the electrolyte.

Fabrication of tungsten ultramicroelectrodes

Disk-type tungsten ultramicroelectrodes (W-UMEs) were fabricated from 25-μm-diameter tungsten wire encapsulated in glass (Supplementary Fig. 1). The glass capillary was locally softened with a flame and pulled around the wire to form a continuous seal, and the rear of the capillary was filled with epoxy before making the electrical connection. After curing, the tip was mechanically polished until a circular tungsten disk was exposed, with the surrounding glass. The nominal electrode radius was 12.5 μm. The exposed disk was inspected optically before use and re-polished after deposition experiments to restore the disk geometry.

Electrochemical measurements and alloy deposition

Linear sweep voltammetry (LSV), galvanostatic measurements, and pulse deposition were performed at room temperature. Three-electrode LSV measurements used the W-UME as the working electrode, a graphite rod as the counter electrode, and an Ag/AgCl reference electrode/quasi-reference electrode. For Ag-containing high-current deposition, a KCl-filled reference electrode was avoided because chloride leakage produced AgCl contamination in preliminary experiments; the W-UME was therefore paired with an Ag/AgCl wire in a two-electrode configuration, and the measured potential is reported versus quasi-Ag/AgCl. When greater material loading was required, short pulses were repeated with intervening rest periods rather than extending a single pulse into the quasi-steady-state regime.

Determination of diffusivity and pulse-design timescales

Ionic diffusivities were obtained from the steady-state limiting current at the disk UME using $i_{ss} = 4nFDCa$, where n is the number of transferred electrons, F is the Faraday constant, D is the diffusion coefficient, C is the bulk concentration, and a is the electrode radius. The interfacial depletion time was calculated from Sand's relation, $t_s = (\pi D/4)(nFC_0/j)^2$, where C_0 is the bulk concentration and j is the applied current density. The onset of efficient radial replenishment was estimated from the characteristic diffusion time across the UME radius. These quantities were used to construct the pulse-design map in Fig. 3C; pulse durations were

selected to exceed the depletion time of the preferentially reduced species while remaining shorter than the radial-replenishment time.

Microscopy sample preparation and characterization

After electrodeposition, the UME tip was rinsed thoroughly with DI water to remove residual electrolyte. For transmission electron microscopy, deposited material was transferred directly into DI water and placed onto lacey-carbon TEM grids. Ethanol was not used during this transfer because carbonaceous residues were repeatedly observed after ethanol-based sample preparation. The grids were dried in a vacuum oven for at least 10 h before analysis. Fe-containing samples were characterized as soon as practicable after preparation to minimize changes associated with oxidation or hydroxide formation. Deposit morphology was examined by scanning electron microscopy (SEM), and elemental distributions were evaluated by energy-dispersive X-ray spectroscopy (EDS). Transmission electron microscopy (TEM), high-resolution TEM (HRTEM), scanning TEM (STEM), and STEM-EDS mapping were used to evaluate particle morphology, crystallinity, and nanoscale elemental distributions. For Fe–Cr, electron energy-loss spectroscopy (EELS) was acquired at multiple positions within individual particles and across different particles to evaluate local compositional uniformity.

CNT–Nafion-supported electrodes and electrocatalytic measurements

A 25um-diameter W-UME and 3mm-diameter glassy-carbon electrode were used for the support-integrated catalyst experiments. SWCNTs and Nafion were dispersed to form a CNT–Nafion ink, which was drop-cast onto the electrode surface and dried to produce a conductive adhesion layer. Cu–Ag was then electrodeposited directly onto the supported electrode. The electrodes were rinsed after deposition and transferred to 0.5 M H_2SO_4 for hydrogen-evolution measurements. Polarization curves were collected at 10 mV s^{-1}.

Data availability

All the data that support the findings of this study are available from the corresponding authors on reasonable request.

Acknowledgements

We acknowledge the use and support of the University of California, Los Angeles, California NanoSystems Institute (UCLA CNSI) EICN Facilities.

Funding

This work was supported by the U.S. Army DEVCOM ARL Army Research Office (ARO) Energy Sciences Competency, Advanced Energy Materials Program award # W911NF-24-1-0369. The views and conclusions contained in this document are those of the authors and should not be interpreted as representing the official policies, either expressed or implied, of the U.S. Army or the U.S. Government. We also acknowledge the support of the National Science Foundation (CBET-2143677)

Author contributions

M.-H.K., J.K.K., and Y.L. conceived the idea and designed the experiments. Y.L. supervised the project. M.-H.K. performed characterization, carried out electrochemical measurements

and analyzed the data. J.K.K., K.L., T.W. and J.K. helped with ultramicroelectrode experiments. H.L. and D.Z. helped with catalysis test. H.P., K.C., and J.T.K. helped with TEM analysis. M.-H.K. and Y.L. wrote the original draft. All coauthors revised and commented on the manuscript.

Competing interests

Authors declare that they have no competing interests.

Supplementary Files

This is a list of supplementary files associated with this preprint. Click to download.

- Supplementaryinfo.pdf